Vibration isolation by relative resonance perceived in combination of rigid bodies and elastic beams

Abhigna Bhatt[a], Somya Ranjan Patro[b], Arnab Banerjee[c]

[a] *Abhigna.Sandipkumar.Bhatt@civil.iitd.ac.in*
[b] *somjan.tro@gmail.com*
[c] *abanerjee@iitd.ac.in*
[d] *Indian Institute of Technology, Civil Engineering Department, Hauz, Khas, Delhi, 110016, India*

Abstract

This paper develops a novel low-frequency vibration isolation device based on rigid body dynamics called a Rigid Elastic Vibration Isolator (REVI). The REVI model is realized by coupling four elastic beams with two rigid bodies monolithically made using 3D printing. The system operates based on the vibration of the intermediate rigid bodies, which leads to the anti-resonance phenomenon at low frequencies. The dynamic analysis of the proposed REVI system has been meticulously investigated through analytical methods and real-world experimentation. The analytical method uses the Spectral element method to obtain the dynamic response, which is also validated by the experimental findings. Furthermore, the REVI transmittance sensitivity analysis was conducted by adjusting the rigid mass and system load and exploring methods for generating wide low-frequency bandgaps. The inclination angle of the REVI system is also varied, revealing the bandgap characteristics regarding negative transmittance level. The parametric study varying the geometric properties of the REVI system enhances our understanding of the bandgap and attenuation characteristics within the attenuation band. The REVI mechanism is practical and easily implemented, allowing for accurate and repeatable modeling. Moreover, the analytical observations assist in refining the shape of the REVI mechanism to achieve the necessary bandgap for the desired transmittance.

Keywords: Vibration isolation, Anti-resonance, Spectral element method, Transmittance, Band-gap

1. Introduction

The demand for vibration isolators is crucial in several real-life applications, such as automobiles [1, 2], helicopter rotors [3–5], machine foundations [6, 7], offshore structures [8, 9], high rise buildings [10, 11], space structures [12] etc. In general, vibration isolation can be easily achieved through passive vibration isolation devices [13] such as base isolation devices [14–17]. However, structures in most civil and mechanical engineering applications are subjected to lower-frequency vibrations [18–20]. This lower frequency vibration isolation can be achieved by designing resonators with lower natural frequency [21–24], i.e., having heavier mass or lower stiffness. However, lower stiffness and heavier mass are difficult to achieve from a stability perspective. Therefore, researchers are inclined toward designing vibration isolators that can work well in lower frequency ranges without increasing their static mass [25–29].

The occurrence of the anti-resonance in the lower frequency range gives rise to a low-frequency stop band, which can be identified from the transmittance plot [30–32] . Recently, researchers have tried to obtain antiresonances using several methods; such as hydraulic leverage [33, 34], levered spring-mass system [35], beams connected by a spring mass system [36–38], inertial amplifier mechanism [14, 39–41], effective negative stiffness [42–44], effective negative mass [45, 46], multi resonating base isolation [16, 38, 47, 48], etc. Besides theoretical studies, several experimental studies have been performed on fabricated isolators such as flexible platforms with rigid mass [49, 50], shape memory alloy spring elements [51], negative stiffness vibration isolator device [52, 53], compliant lever-type passive vibration isolators [54]etc.

Fabricating a vibration isolating device with attached resonating units is always challenging. Few researchers have fabricated the inertial amplifier [55] and negative stiffness devices [56] for low-frequency vibration isolation. The fabrication of pinned connections and rigid mass-less bars are the two prime intricacies associated with the manufacturing process of inertial amplifier devices. Often, slender beams are used at the junction and the thick section at the middle part to replicate the inertial amplifier [57]. However, the stress concentration in slender beams is very high in these devices. Additionally, jointed parts may get dislocated due to high amplitude vibration in a resonating device that connects springs and masses. [58, 59].

Due to the intricate forms of many vibration isolation mechanisms, 3D printing is now widely used in manufacturing [60–62] due to repeatability and dimensional precision [55, 63, 64]. The monolithic model creation using 3D printing technology has reduced the number of joints in a structure and the geometrical uncertainties of physical modeling. In this paper, the rigid elastic vibration isolator (REVI) model has been developed using 3D printing technology. The proposed REVI could be confused with a negative stiffness [46, 65] or an inertial amplifier model due to geometric resemblance; however, the working mechanism of REVI and its intrinsic properties are very different. For the analytical study of this REVI model, its dynamic stiffness matrix has been developed using spectral element matrix and rigid body dynamics [66–68]. The natural frequency of the developed REVI model has been obtained by experimental investigation, which has been used to compute the rotational stiffness of the beam joint. Further incorporating the rotational stiffness, the modified dynamic stiffness matrix has been obtained. The transmittance of REVI has been found experimentally, validating the analytical model developed. The primary novelty of the paper lies in fabricating a monolithic vibration isolator that uses the concept of rigid body dynamics and anti-resonance for broadband vibration isolation. Finally, a parametric study by varying nodal masses has been performed to gain insight into the physics behind antiresonance occurrence in transmittance. Additionally, a detailed study of change in transmittance level due to variation in geometric design has been carried out, which illustrated that the proper geometric design of REVI can create a double antiresonance peak in transmittance level, which results in a wider bandgap with required vibration transmittance.

This manuscript is organized as follows. Following this introduction, in section 2, a detailed procedure is provided for fabricating the REVI system and an analytical algorithm to formulate the dynamic stiffness matrix using the spectral element method. section 3 provides a detailed procedure to estimate the rotational stiffness of the semi-rigid joint of the REVI system experimentally. section 4 describes the complete analytical and experimental procedure for obtaining the transmittance. A comparison study of the transmittance parameters obtained from both analytical and experimental is shown in section 5. Additionally, a few parametric studies were conducted to evaluate the band-gap characteristics for different geometric parameters of the REVI system, such as mass ratio, inclination angle, etc. Finally, the conclusion from the findings is summarized in section 6.

2. Theoretical analysis and design of REVI

This section provides a detailed procedure to fabricate the REVI model and a complete analytical algorithm to formulate the dynamic stiffness matrix using the spectral element method.

Table 1: Material and Geometrical properties

Apparatus	Property	Symbols	Units	Values
PLA material	Density	ρ	kg/m^3	778.89
	Young's modulus	E	GPa	2.9
Elastic beam	Length	l	m	0.0453
	Width	b	m	0.01
	Thickness	d	m	0.001
	Cross-sectional area	$A = bd$	m^2	10^{-5}
	Second moment of area	$I = bd^3/12$	m^4	$8.33x10^{-13}$
Rigid mass	Length	l	m	0.01
	Width	b	m	0.01
	Thickness	d	m	0.01
	Mass	$m_r = bdl\rho$	kg	$7.889x10^{-4}$
	Polar moment of inertia	$J_r = m_r d^2/6$	kg/m^2	$1.298x10^{-8}$
Force transducer	Sensitivity	–	mV/kN	2248
	Mass	M_f	kg	0.02697
Two accelerometers	Sensitivity	–	mV/(m/s^2)	4.98
	Mass	M_a	kg	0.0236

2.1. REVI model fabrication

The CAD model of the proposed REVI is made in AutoCAD software, which is then converted to a .gcode file using Ultimaker Cura software (Figure 1 (a)). The .gcode file is then printed in the 3D printing device (Ender) with the help of additive manufacturing technology (Figure 1 (b)). The monolithic 3D printed REVI model is demonstrated in Figure 1 (c). The material used for the REVI model is polylactic acid (PLA), whose density was calculated by finding the sample's ratio of mass and volume. The model and sensors' overall material and geometric properties have been described in Table 1.

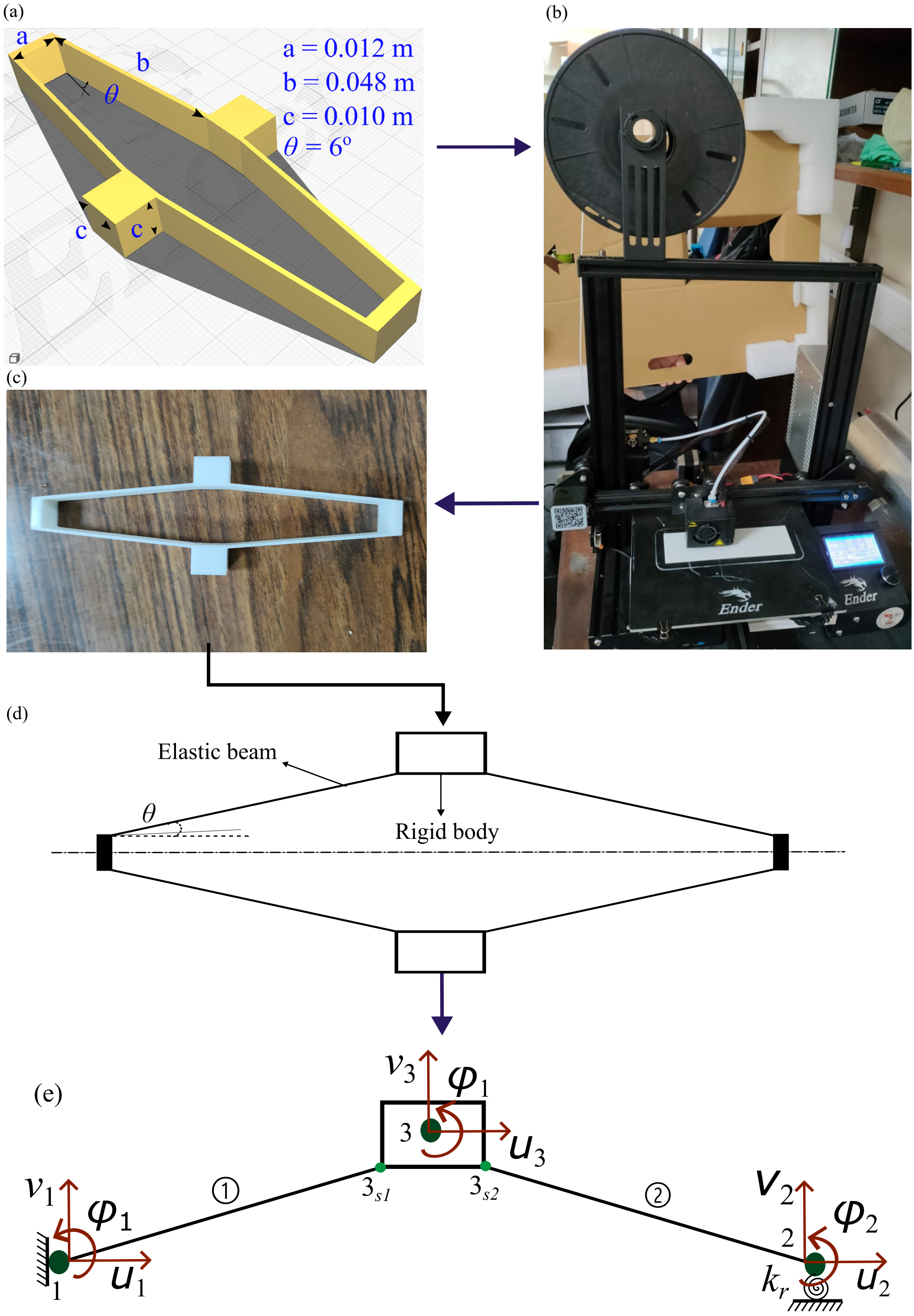

Figure 1: (a) CAD model of the REVI ; (b) 3D printing device; (c) 3D printed proposed REVI; (d) Analytically modeled REVI and (e) Degrees of freedom and boundary conditions at each node

2.2. Analytical model development

The REVI model is realized by coupling four elastic beams with two rigid bodies, as shown in Figure 1 (d). Exploiting the symmetry of this system, The analysis of only half part (shown in Figure 1 (e)) of the REVI has been carried out. Rigid body dynamics and spectral element techniques are used to obtain the global dynamic stiffness matrix [68]. The elastic beams are slender and assumed to follow the Euler-Bernoulli beam theory. The beams are modeled as frame elements, with three degrees of freedom in each node: axial, transverse, and rotational. To obtain the dynamic properties of the entire system, the REVI is subjected to input base excitation at one end. The output dynamic response at the other end is obtained regarding displacement. The details on the mathematical formulation of the dynamic stiffness matrix are provided in the subsequent sections.

2.2.1. Spectral element matrix in local coordinate system

The governing differential equation of motion (GDEM) for i^{th} beam element vibrating along the transverse direction can be expressed as follows,

$$EI\frac{\partial^4 v\left(x,t\right)}{\partial x^4}+\rho A\frac{\partial^2 v\left(x,t\right)}{\partial t^2}=0 \tag{1}$$

and for axial direction, the GDEM can be defined as

$$E\frac{\partial^2 u\left(x,t\right)}{\partial x^2}-\rho\frac{\partial^2 u\left(x,t\right)}{\partial t^2}=0 \tag{2}$$

Here, w and u represent the transverse and axial displacement of the i^{th} beam, which depends on the spatial coordinate (x) and time (t). The parameters EI and ρA denote the beam's flexural rigidity and mass per unit length. A harmonic solution for the governing equation described above can be derived through the variable separable method for transverse direction, i.e.,

$$v\left(x,t\right)=V\left(x\right)\mathrm{e}^{-\mathrm{i}\omega t} \tag{3}$$

and, for axial direction, i.e.,

$$u\left(x,t\right)=U\left(x\right)\mathrm{e}^{-\mathrm{i}\omega t} \tag{4}$$

Here, $V(x)$ and $U(x)$ represent the amplitude of transverse and axial displacement of the i^{th} beam as a function of the spatial coordinate alone, and ω is the frequency of the excitation. By substituting equation Eq. (3) and Eq. (4) into equation Eq. (1) and Eq. (2), the differential equations can be transformed into the spatial domain as follows:

$$EI\frac{\partial^4 V(x)}{\partial x^4} - \omega^2 \rho A V(x) = 0 \tag{5}$$

and,

$$E\frac{\partial^2 U(x)}{\partial x^2} + \omega^2 \rho U(x) = 0 \tag{6}$$

Under the assumption of a uniform section, where both EI and ρA remain constant along the entire length of the beam, the transverse solution to the given equation can be expressed using hyperbolic trigonometric functions.

$$V(x) = A_1 \sin(\lambda x) + A_2 \cos(\lambda x) + A_3 \sinh(\lambda x) + A_2 \cosh(\lambda x) \tag{7}$$

and similarly, the solutions for the axial directions can be obtained as

$$U(x) = B_1 \sin(\mu x) + B_2 \cos(\mu x) \tag{8}$$

where, A_1 through A_4, B_1 and B_2 represent unknown arbitrary constants. λ and μ represent the wave numbers for transverse and axial direction. By substituting equation Eq. (7) and Eq. (8) into equation Eq. (5) and Eq. (6), the wave numbers λ and μ can be expressed as a function of the excitation frequency ω as follows:

$$EI\lambda^4 V(x) - \omega^2 \rho A V(x) = 0 \Rightarrow \lambda = \sqrt[4]{\frac{\omega^2 \rho A}{EI}} \tag{9}$$

and

$$-EA\mu^2 U(x) + \omega^2 \rho A U(x) = 0 \Rightarrow \mu = \sqrt{\frac{\omega^2 \rho}{E}} \tag{10}$$

The state vectors at a single end of i^{th} beam element, specifically rotation (ϕ), axial force (P), bending moment (M), and shear force (V), can be expressed in terms of the transverse displacement (w) and axial displacement (u) as

$$\begin{aligned} &\phi(x,t) = V^I(x)\,\mathrm{e}^{-\mathrm{i}\omega t}, F_x(x,t) = EAU^I(x)\,\mathrm{e}^{-\mathrm{i}\omega t}, \\ &M(x,t) = EIV^{II}(x)\,\mathrm{e}^{-\mathrm{i}\omega t}, F_y(x,t) = EIV^{III}(x)\,\mathrm{e}^{-\mathrm{i}\omega t} \end{aligned} \tag{11}$$

Substituting Eq. (7) and Eq. (8) in Eq. (11), the displacement state vectors for i^{th} beam element shown in Figure 1 (e) can be defined as

$$\mathbf{D} = \mathbf{H}\boldsymbol{\Theta} \Rightarrow \boldsymbol{\Theta} = \mathbf{H}^{-1}\mathbf{D} \tag{12}$$

where,
$\mathbf{D}_j = \left\{ \begin{array}{cccccc} u_i & v_i & \phi_i & u_{i+1} & v_{i+1} & \phi_{i+1} \end{array} \right\}^T$, $\boldsymbol{\Theta} = \left\{ \begin{array}{cccccc} B_1 & A_1 & A_2 & B_2 & A_3 & A_4 \end{array} \right\}^T$ and

$$\mathbf{H}_j = \begin{bmatrix} 0 & 0 & 0 & 1 & 0 & 0 \\ 0 & 0 & 1 & 0 & 0 & 1 \\ 0 & \lambda & 0 & 0 & \lambda & 0 \\ \sin(\mu l) & 0 & 0 & \cos(\mu l) & 0 & 0 \\ 0 & \sin(\lambda l) & \cos(\lambda l) & 0 & \sinh(\lambda l) & \cosh(\lambda l) \\ 0 & \lambda\cos(\lambda l) & -\lambda\sin(\lambda l) & 0 & \lambda\cosh(\lambda l) & \lambda\sinh(\lambda l) \end{bmatrix} \tag{13}$$

Here, l is the length of the i^{th} beam element. Similarly, the force state vectors for i^{th} beam element shown in Figure 1 (e) can be defined as

$$\mathbf{F}_j = \mathbf{X}_j\mathbf{K}_j\Theta \tag{14}$$

where, $\begin{array}{l} \mathbf{F}_j = \left\{ \begin{array}{cccccc} F_{xi} & F_{yi} & M_i & F_{x(i+1)} & F_{y(i+1)} & M_{i+1} \end{array} \right\}^T \\ = \left\{ \begin{array}{cccccc} F_{xi}(0) & F_{yi}(0) & M_i(0) & F_{x(i+1)}(L_j) & F_{y(i+1)}(L_j) & M_{i+1}(L_j) \end{array} \right\}^T \end{array}$. Here, $\mathbf{X}_i$ and $\mathbf{K}_i$ can be defined as

$$\mathbf{X}_j = \begin{bmatrix} -EA & 0 & 0 & 0 & 0 & 0 \\ 0 & EI & 0 & 0 & 0 & 0 \\ 0 & 0 & -EI & 0 & 0 & 0 \\ 0 & 0 & 0 & EA & 0 & 0 \\ 0 & 0 & 0 & 0 & -EI & 0 \\ 0 & 0 & 0 & 0 & 0 & EI \end{bmatrix} \tag{15}$$

and,

$$\mathbf{K}_j = \begin{bmatrix} \mu & 0 & 0 & 0 & 0 & 0 \\ 0 & -\lambda^3 & 0 & 0 & \lambda^3 & 0 \\ 0 & 0 & -\lambda^2 & 0 & 0 & \lambda^2 \\ \mu\cos(\mu L_j) & 0 & 0 & -\mu\sin(\mu L_j) & 0 & 0 \\ 0 & -\lambda^3\cos(\lambda L_j) & \lambda^3\sin(\lambda L_j) & 0 & \lambda^3\cosh(\lambda L_j) & \lambda^3\sinh(\lambda L_j) \\ 0 & -\lambda^2\sin(\lambda L_j) & -\lambda^2\cos(\lambda L_j) & 0 & \lambda^2\sinh(\lambda L_j) & \lambda^2\cosh(\lambda L_j) \end{bmatrix} \tag{16}$$

Substituting Eq. (12) in Eq. (14), the force-displacement relationship between the two ends of of the i^{th} beam element can be defined as

$$\mathbf{F}_j = \mathbf{X}_j\mathbf{K}_j\Theta = \mathbf{X}_j\mathbf{K}_j{\mathbf{H}_j}^{-1}\mathbf{D}_j = \mathbf{S}_j\mathbf{D}_j \tag{17}$$

Here, $\mathbf{S}_j$ is the dynamic stiffness matrix, also known as the Spectral element matrix of the i^{th} beam element, which can be expressed as

$$\mathbf{S}^i = \begin{bmatrix} s_{11} & 0 & 0 & s_{14} & 0 & 0 \\ 0 & s_{22} & s_{23} & 0 & s_{25} & s_{26} \\ 0 & s_{32} & s_{33} & 0 & s_{35} & s_{36} \\ s_{41} & 0 & 0 & s_{44} & 0 & 0 \\ 0 & s_{52} & s_{53} & 0 & s_{55} & s_{56} \\ 0 & s_{62} & s_{63} & 0 & s_{65} & s_{66} \end{bmatrix} \tag{18}$$

where,

$$\begin{aligned}
s_{11} = s_{44} &= \frac{EA\,\mu\,\cos(\mu\,l_i)}{\sin(\mu\,l_i)} \\
s_{14} = s_{41} &= -\frac{EA\,\mu}{\sin(\mu\,l_i)} \\
s_{22} = s_{55} &= -\frac{EI\,\lambda^3\,(\cosh(\lambda\,l_i)\sin(\lambda\,l_i) + \cos(\lambda\,l_i)\sinh(\lambda\,l_i))}{\cos(\lambda\,l_i)\cosh(\lambda\,l_i) - 1} \\
s_{23} = -s_{56} &= -\frac{EI\,\lambda^2\sin(\lambda\,l_i)\sinh(\lambda\,l_i)}{\cos(\lambda\,l_i)\cosh(\lambda\,l_i) - 1} \\
s_{25} &= \frac{EI\,\lambda^3\,(\sinh(\lambda\,l_i) + \sin(\lambda\,l_i))}{\cos(\lambda\,l_i)\cosh(\lambda\,l_i) - 1} \\
s_{26} = -s_{35} &= \frac{EI\,\lambda^2\,(\cos(\lambda\,l_i) - \cosh(\lambda\,l_i))}{\cos(\lambda\,l_i)\cosh(\lambda\,l_i) - 1} \\
s_{33} = s_{66} &= \frac{EI\,\lambda\,\,(\cos(\lambda\,l_i)\sinh(\lambda\,l_i) - \cosh(\lambda\,l_i)\sin(\lambda\,l_i))}{\cos(\lambda\,l_i)\cosh(\lambda\,l_i) - 1} \\
s_{36} &= \frac{EI\,\lambda\,\,(\sin(\lambda\,l_i) - \sinh(\lambda\,l_i))}{\cos(\lambda\,l_i)\cosh(\lambda\,l_i) - 1}
\end{aligned}$$

The displacement continuity equations and force equilibrium equations are used to derive the relation between primary node 3 (center of the rigid body) and secondary node 3_{si} (beam's node connected to the rigid body). For beam i, X_i and Y_i are distances between master node 3 and slave node 3_{si} in global coordinates. Beam's local axis system makes an angle θ_i with the global axis. The distances x_i and y_i in the local coordinate system are derived as

$$\begin{bmatrix} x_i \\ y_i \end{bmatrix} = \begin{bmatrix} \cos(\theta_i) & -\sin(\theta_i) \\ \sin(\theta_i) & \cos(\theta_i) \end{bmatrix} \begin{bmatrix} X_i \\ Y_i \end{bmatrix} \tag{19}$$

The dynamic stiffness matrix of i^{th} beam incorporating the second node at the center of gravity of a rigid body can be defined as

$$\mathbf{R}^i = \mathbf{T}_{rd}\,\mathbf{S}^i\,\mathbf{T}_{rd}^T \tag{20}$$

where,

$$\mathbf{T}_{rd} = \begin{bmatrix} 1 & 0 & 0 & 0 & 0 & 0 \\ 0 & 1 & 0 & 0 & 0 & 0 \\ 0 & 0 & 1 & 0 & 0 & 0 \\ 0 & 0 & 0 & 1 & 0 & y_i \\ 0 & 0 & 0 & 0 & 1 & -x_i \\ 0 & 0 & 0 & 0 & 0 & 1 \end{bmatrix} \tag{21}$$

2.2.2. Spectral element matrix in global coordinate system

Further, the dynamic stiffness matrix in the local coordinate system $\mathbf{R}_i$ is transformed into a global coordinate system by coordinate transformation matrix $\mathbf{T}$ as

$$\mathbf{K}^i = \mathbf{T}\,\mathbf{R}^i\,\mathbf{T}^T \tag{22}$$

where,

$$\mathbf{T} = \begin{bmatrix} \cos(\theta_i) & \sin(\theta_i) & 0 & 0 & 0 & 0 \\ -\sin(\theta_i) & \cos(\theta_i) & 0 & 0 & 0 & 0 \\ 0 & 0 & 1 & 0 & 0 & 0 \\ 0 & 0 & 0 & \cos(\theta_i) & \sin(\theta_i) & 0 \\ 0 & 0 & 0 & -\sin(\theta_i) & \cos(\theta_i) & 0 \\ 0 & 0 & 0 & 0 & 0 & 1 \end{bmatrix} \tag{23}$$

The force-displacement relation for beam 1 can be written as

$$\begin{Bmatrix} \mathbf{F}_1 \\ \mathbf{F}_3 \end{Bmatrix} = \begin{bmatrix} \mathbf{K}_{11}^1 & \mathbf{K}_{13}^1 \\ \mathbf{K}_{31}^1 & \mathbf{K}_{33}^1 \end{bmatrix} \begin{Bmatrix} \mathbf{U}_1 \\ \mathbf{U}_3 \end{Bmatrix} \tag{24}$$

Similarly, the force-displacement relation for beam 2 can be written as

$$\begin{Bmatrix} \mathbf{F}_2 \\ \mathbf{F}_3 \end{Bmatrix} = \begin{bmatrix} \mathbf{K}_{22}^2 & \mathbf{K}_{23}^2 \\ \mathbf{K}_{32}^2 & \mathbf{K}_{33}^2 \end{bmatrix} \begin{Bmatrix} \mathbf{U}_2 \\ \mathbf{U}_3 \end{Bmatrix} \tag{25}$$

where, $\mathbf{U}_j$ is displacement vector and $\mathbf{F}_j$ is force vector of j^{th} node as

$$\mathbf{U}_j = \begin{Bmatrix} u_j \\ v_j \\ \phi_j \end{Bmatrix} \quad \mathbf{F}_j = \begin{Bmatrix} F_{xj} \\ F_{y_j} \\ M_j \end{Bmatrix} \tag{26}$$

2.2.3. Assembly

Due to inertial mass in the axial and transverse direction, the inertial force matrix and polar moment of inertia in the rotational degree of freedom must be added at corresponding nodes. Let m_j and J_j be the mass and polar moment of inertia at j^{th} node. The inertial force matrix is written as

$$\mathcal{I}_j = -\,\omega^2 \underbrace{\begin{bmatrix} m_j & 0 & 0 \\ 0 & m_j & 0 \\ 0 & 0 & J_j \end{bmatrix}}_{\mathbf{I}_j} \mathbf{U_j} \tag{27}$$

The final assembled dynamic stiffness matrix of the system in global coordinates can be written as

$$\begin{Bmatrix} \mathbf{F}_1 \\ \mathbf{F}_2 \\ \mathbf{F}_3 \end{Bmatrix} = \underbrace{\begin{bmatrix} \mathbf{K}^1_{11} - \mathbf{I}_1 & 0 & \mathbf{K}^1_{13} \\ 0 & \mathbf{K}^2_{22} - \mathbf{I}_2 & \mathbf{K}^2_{23} \\ \mathbf{K}^1_{31} & \mathbf{K}^2_{32} & \mathbf{K}^1_{33} + \mathbf{K}^2_{33} - \mathbf{I}_3 \end{bmatrix}}_{\bar{\mathbf{K}}} \begin{Bmatrix} \mathbf{U}_1 \\ \mathbf{U}_2 \\ \mathbf{U}_3 \end{Bmatrix} \tag{28}$$

2.2.4. Boundary condition

The analytical model exploits the symmetricity of the system, which restrains the degree of freedom in the v direction for node 1 and 2, i.e., $v_1 = v_2 = 0$. Node 1 will be fixed with the base plate, which can move only in the u direction, so the rotational degree of freedom at node 1 will be restrained, so $\phi_1 = 0$. However, at node 2, the rotational degree of freedom is not fully restrained. Therefore, the rotational spring of stiffness k_r is modeled at the node 2. Therefore, the rotational spring with stiffness k_r has been modeled at node 2. Therefore, the rotational spring stiffness k_r will be added in the global dynamic stiffness matrix ($\bar{\mathbf{K}}$) at the stiffness coefficient corresponding to moment and rotation at node 2 as

$$\bar{\mathbf{K}}(6,6) = \bar{\mathbf{K}}(6,6) + k_r \tag{29}$$

The boundary conditions of this system are defined as

$$\begin{aligned} v_1 = \phi_1 &= 0 \\ v_2 &= 0 \\ M_2 &= k_r\,\phi_2 \end{aligned} \tag{30}$$

After applying the boundary conditions, the reduced force-displacement equation can be written as

$$\begin{bmatrix} F_{x1} \\ F_{x2} \\ M_2 \\ F_{x3} \\ F_{y3} \\ M_3 \end{bmatrix} = \bar{\mathbf{K}}_{bc} \begin{bmatrix} u_1 \\ u_2 \\ \phi_2 \\ u_3 \\ v_3 \\ \phi_3 \end{bmatrix} \tag{31}$$

where, the reduced stiffness matrix ($\bar{\mathbf{K}}_{bc}$) has been derived in Appendix A.

3. Estimation of rotational stiffness k_r

While the rotational degree of freedom is fully restrained, the rotational stiffness k_r is infinite; however, the rotational stiffness value zero indicates free rotation. As node 2 is a semi-rigid joint, the value of its rotational stiffness k_r will be between 0 to ∞, which needs to be obtained experimentally. In this paper, the experiment has been carried out to find the system's natural frequency and equate it with the analytical natural frequency of the same mode to determine the rotational stiffness k_r of the joint.

3.1. Experimental setup for determining natural frequency

The natural frequency of the REVI can be estimated by fixing it to a fixed base situated at a certain height, and an accelerometer was attached at the bottom of the sample. Small displacement was provided at the bottom in a vertical direction, allowing the model to vibrate freely (Figure 2 (a)). The vertical acceleration vs. time was recorded as shown in Figure 2 (b), which is then converted to the frequency domain using the Fast Fourier Transform (FFT) algorithm (Figure 2 (c)). The FFT graph's maximum amplitude is the REVI's natural frequency, i.e., 92 Hz ($\omega_n = 578.05$ rad/s).

3.2. Determining natural frequency analytically

Nodal masses and boundary conditions are similar to the experimental setup and have been applied in the Eq. (31) to determine the natural frequency. One side of the designed REVI has been fixed at the top, and the other is free to move. Therefore, The inertia matrix ($\mathbf{I}_1$) at node 1 is zero as no additional mass is attached. Further, the attached accelerometer at the bottom is modeled as a point mass at node 2. $m_2 = m_a/2$ (m_2 is half of the accelerometer mass due to symmetric condition), and $J_2 = 0$ has been used in the inertia matrix $\mathbf{I}_2$. The inertia matrix at node 3 will have mass ($m_3 = m_r$) and polar moment of inertia ($J_3 = J_r$) as calculated for a rigid body in Table 1.

The node 1 is fixed at the top, restraining the displacement in the u direction, thus incorporating the boundary condition $u_1 = 0$ in Eq. (31). Further, by static condensation the reduced matrix $\bar{\mathbf{K}}_{bc1}(\omega, k_r)$ has been obtained Appendix B. The determinant of the dynamic stiffness matrix will be zero at its natural frequency.

$$|\bar{\mathbf{K}}_{bc1}(\omega_n, k_r)| = 0 \tag{32}$$

The analytical natural frequency for free rotation ($k_r = 0$) and restrained rotation ($k_r = \infty$) has been obtained as 73.21 Hz and 100.27 Hz, respectively. It validates that the experimental natural frequency lies within the natural frequency obtained analytically, 73.21 to 100.27 Hz. Therefore, applying this concept, the rotational spring stiffness k_r is obtained in Figure 3 by varying k_r. The $|\bar{\mathbf{K}}_{bc}(\omega_n, k_r)|$ is found zero at rotational stiffness $k_r = 0.3591$ Nm/rad.

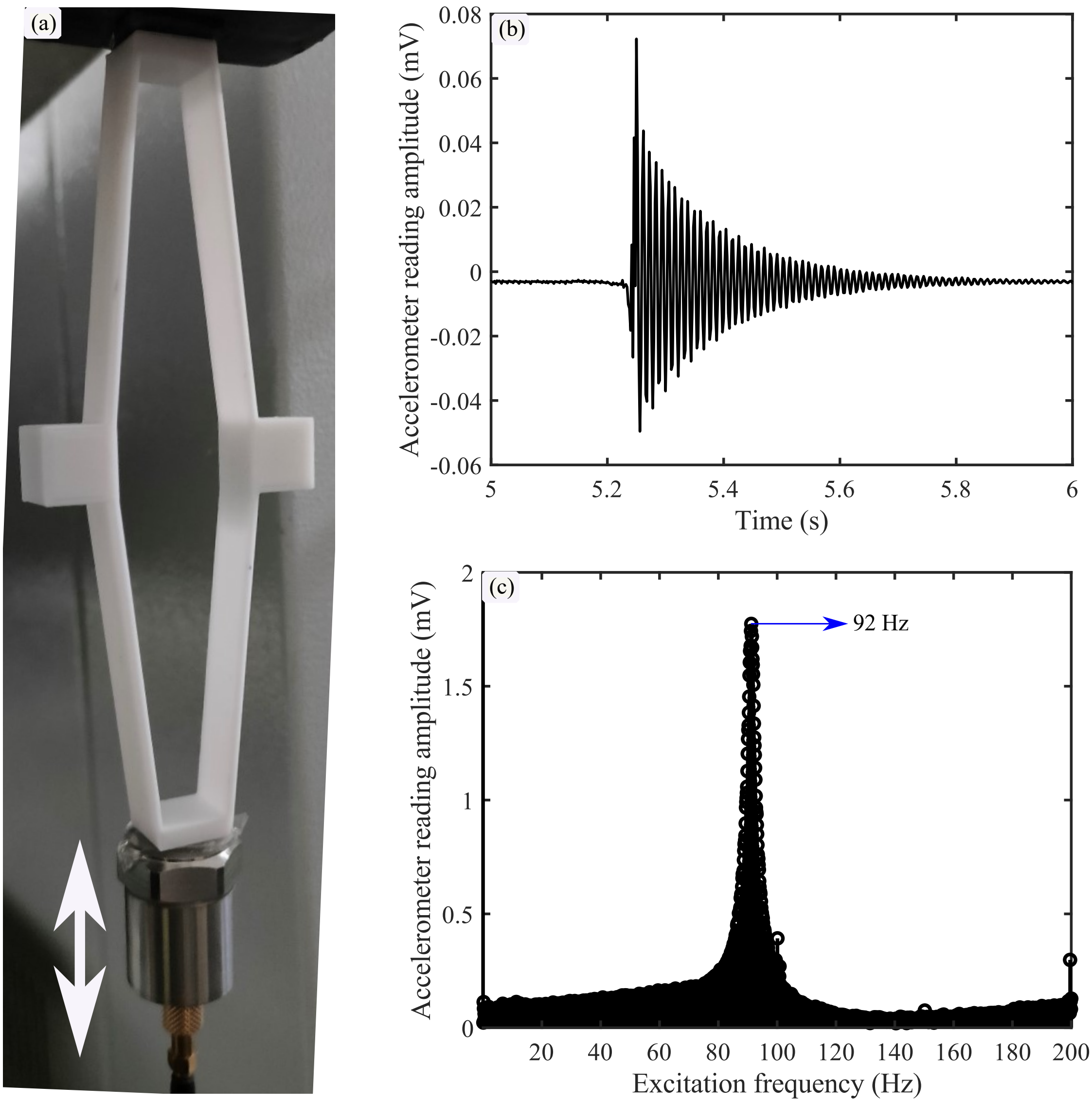

Figure 2: (a) Free vibration of REVI model for estimation of natural frequency; (b) Time acceleration plot of the free vibration analysis; (c) Frequency domain plots with the help of FFT algorithm (sensitivity of accelerometer = 4.98 mV/ms^{-2})

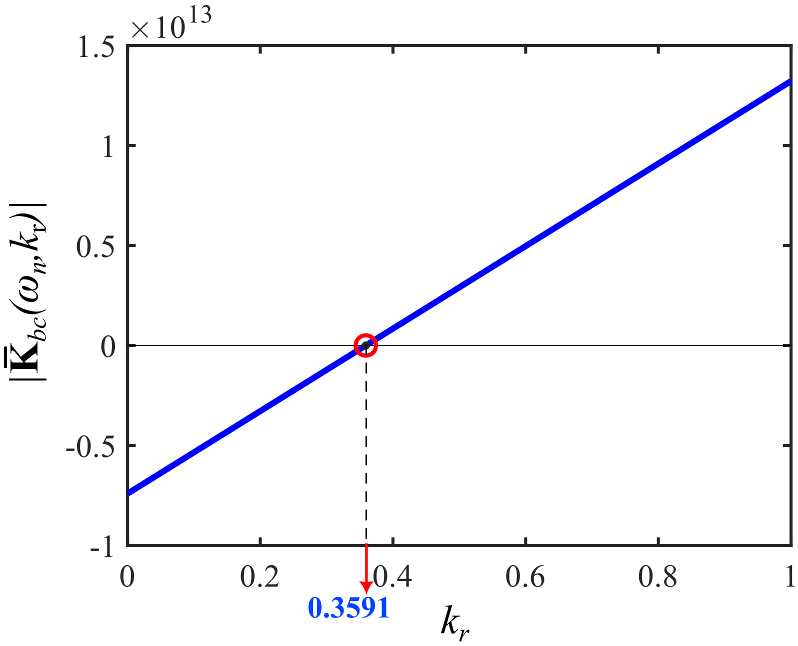

Figure 3: Plot of determinant of dynamic stiffness matrix for natural frequency $\omega_n = 578.05$ rad/s with rotational spring stiffness k_r. The zero determinant is shown by a circle marker at the rotational stiffness $k_r = 0.3591$ Nm/rad.

3.3. Natural Modal shapes

The REVI model has been simulated in COMSOL software, incorporating geometric and material properties outlined in Table 1 and utilizing the rotational stiffness (k_r) determined in Figure 3. The model considered in the COMSOL software is the same as in the analytical model due to its symmetricity, as shown in Figure 1 (d). The results include the natural frequencies and their corresponding modal shapes, as illustrated in Figure 4 (a-c). Additionally, analytically obtained natural frequencies are presented in Figure 4 (d) through a plot of $\log_{10}(|(\mathbf{K}_{bc})|)$ against frequency. This representation effectively highlights the occurrence of spikes at natural frequencies, where the determinant of the spectral element matrix becomes zero. The negligible difference between analytically derived and COMSOL-generated natural frequencies serves as a validation of the model. The modal shapes depicted in Figure 4 (a-c) provide insights into the vibration mechanism of the model..

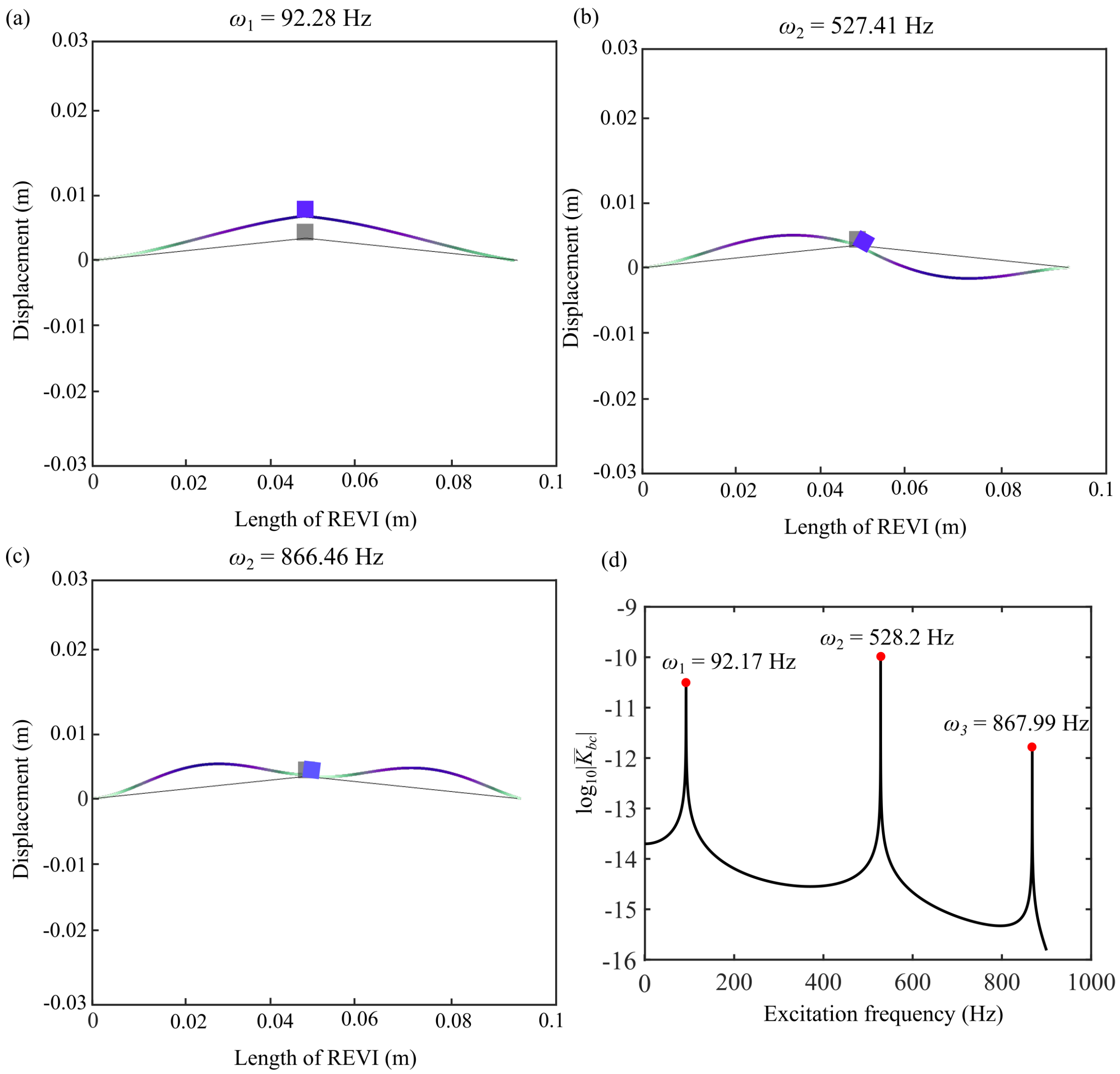

Figure 4: (a) First, (b) Second and (c) Third modal shapes of REVI and (d) Logarithm of the determinant of spectral element matrix ($\mathbf{K}_{bc}$) of REVI.

4. Estimation of vibration isolation performance

The vibration isolation performance is estimated from the vibration transmittance from the base to the system. The transmittance in the u direction between node 1 and 2 has been obtained analytically and experimentally for validation.

4.1. Experimental procedure for transmittance computation

This section shows the detailed experimental procedure to compute the transmittance. Thus, this section is further subdivided into two parts, i.e., experimental setup, which shows the complete procedure of setting up the REVI to the dynamic shaker, and post-processing, which elucidates the detailed procedure of obtaining the transmittance.

4.1.1. Experimental setup

As shown in Figure 5 (b), the experimental setup consists of a PLA rigid beam whose one end is fixed with the base plate of the dynamic shaker, and the other is attached to the REVI model. A force transducer of sensitivity 2248 mV/kN is connected between the rigid beam and the REVI model (Figure 5 (b)) to record the amount of reaction force generated due to the vibration of REVI. Two accelerometers (A_1 and A_2) having a sensitivity of 4.98 mV/ms^{-2} have been placed at the top and bottom of the REVI to measure the transmittance as shown in Figure 5 (b). The accelerometers and force transducer are connected in the corresponding channels of the data acquisition system (DAQ) as shown in Figure 5 (c). The DAQ is then connected to the PC interface, which converts the continuous analog signals to discrete analog signals, which can be simulated through LabView software (Figure 5 (d)). With the aid of a power amplifier (Figure 5 (a)), desired frequency values and voltage gain are provided to the dynamic shaker, which converts electrical energy to mechanical energy and produces a harmonic excitation at the base plate of the shaker system. The whole setup is configured to vibrate vertically.

4.1.2. Post processing of the measured raw data

The dynamic shaker provides monochromatic harmonic sinusoidal base excitation to the REVI. The frequency range is varied from 20 Hz to 160 Hz. The LabView software obtains the time vs. amplitude graphs in millivolt (mV). The raw data for each frequency has been acquired after waiting a few seconds to allow the system to vibrate steadily. The time vs. force in Newton (N) and time vs. acceleration in m/s^2 are obtained from the force transducers and accelerometers using the sensitivity values given in Table 1 as shown in Figure 5 (e) to Figure 5 (g). The frequency domain plots of the corresponding time domain plots can be obtained through the FFT algorithm as shown in Figure 5 (h) to Figure 5 (j). The ratio of frequency amplitude of the bottom accelerometer (A_2) to the top accelerometer (A_1), also known as transmittance (T_r) for the above frequency range, is compared with the corresponding analytical methods shown in Figure 6.

4.2. Analytically obtaining transmittance

In this setup, the force transducer is attached to node 1, the accelerometer is attached to node 2, and the rigid body of PLA is at node 3. The nodal masses and polar moment of inertia at node 1, 2 and 3 due to force transducer, accelerometer, and rigid body will be accounted as $m_1 = M_f/2$, $J_1 = 0$, $m_2/2 = m_a$, $J_2 = 0$ and $m_3 = m_r$, $J_3 = J_r$ (Table 1).

Here, node 1 is fixed at the base plate of the beam connected to the shaker. The displacement of node 1 will be the same as the rigid beam end due to the vibrating shake base plate. The rigid beam is vibrating only in u directional degree of freedom. As the system is assumed to be in the linear range, the base displacement boundary condition $u_1 = 1$ can be assumed for all the frequencies. Applying base excitation boundary condition by static

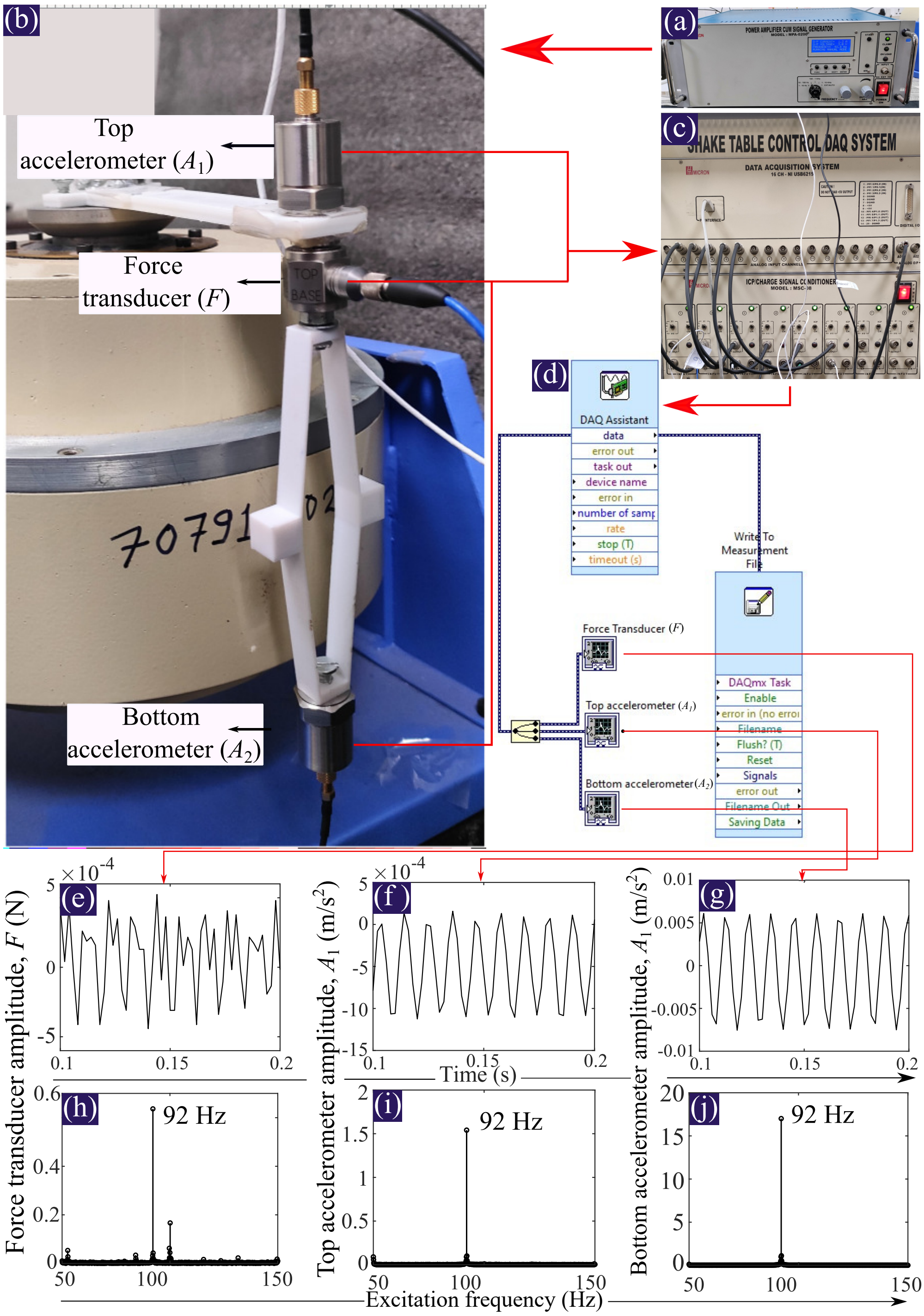

Figure 5: (a) Power amplifier to vibrate the shaker system at desired gain and frequency; (b) REVI connected to the dynamic shaker system; (c) DAQ device used to collect the response of accelerometers and force transducers; (d) Simulation of data acquisition system using LabView software; (e) to (j) Time and frequency domain response of force transducers and accelerometers at a frequency of 92 Hz.

condensation to Eq. (31), the reduced Force displacement equation can be determined as given in Appendix C.

The transmittance of vibration in u direction of base (node 1) u_1, to the accelerometer (node 2) u_2 can be obtained by

$$T_r = \log_{10}\left(\frac{u_2}{u_1}\right) \tag{33}$$

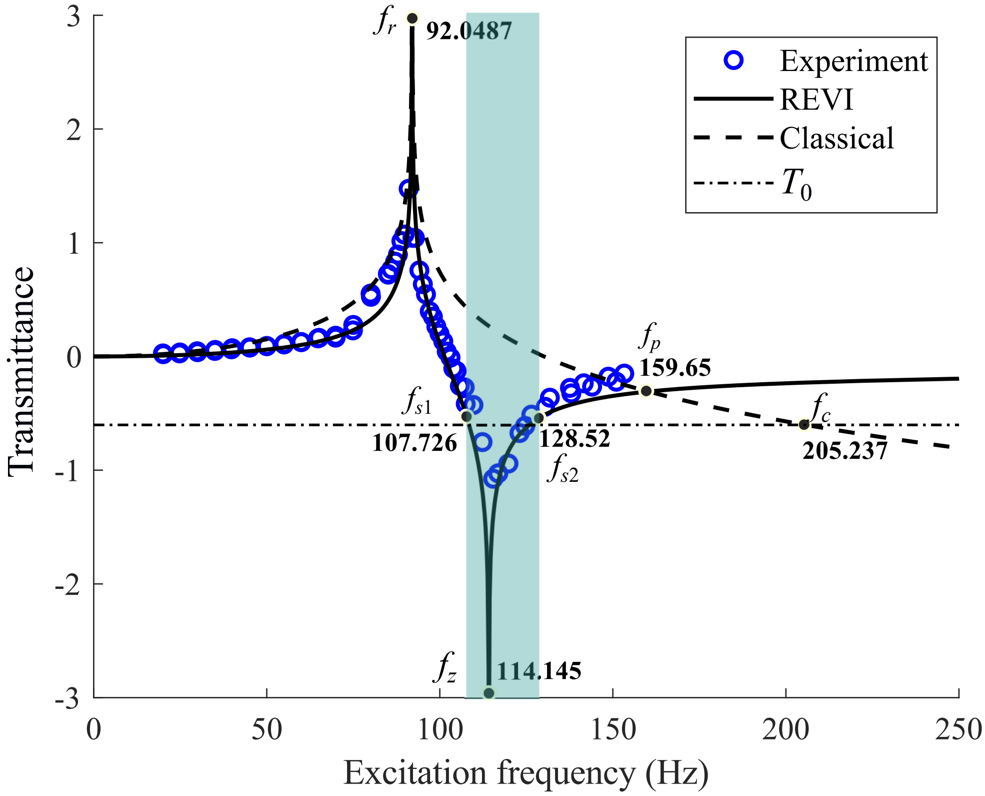

Figure 6: Transmittance of the proposed REVI system from experimental and analytical computation compared to an equivalent spring-mass system. The REVI system's bandwidth (shaded region) is 0.1767 for one-fourth amplitude transmittance.

5. Results and discussions

The transmittance of REVI has been compared with the classical spring mass resonator of a similar natural frequency (92 Hz). In equivalent classical resonator; keeping the mass ($M_c = M_2$), the equivalent spring stiffness (K_c) of classical resonator has been obtained as

$$K_c = \omega_n^2 M_c \tag{34}$$

The transmittance of the classical resonator can be obtained as

$$T_c = \log_{10}\left(\left|\frac{K_c}{K_c - \omega^2\, M_c}\right|\right) = \log_{10}\left(\left|\frac{1}{1-(\omega^2/\omega_r^2)}\right|\right) \tag{35}$$

The transmittance obtained for REVI using Eq. (33) and classical resonator using Eq. (35) is plotted in Figure 6 in solid and dashed lines, respectively. The transmittance peak occurs at resonance frequency ($f_r = 92.0487\,\text{Hz}$). However, an anti-resonance dip is obtained in REVI at ($f_z = 114.145\,\text{Hz}$). The transmittance of REVI is less than the classical resonator till ($f_p = 159.65\,\text{Hz}$) as shown in Figure 6. Generally, any system's allowable transmittance (T_0) is given. Let the allowable transmittance be ($T_0 = \log_{10} 0.25$). Therefore the black dashed line shown in Figure 6 shows logarithmic transmittance level, which cuts transmittance of REVI at ($f_{s1} = 107.726\,\text{Hz}$) and ($f_{s2} = 128.52\,\text{Hz}$) and classical resonator at ($f_c = 205.237\,\text{Hz}$). The frequency ranges f_{s1} to f_{s2} demonstrates the stop band for the REVI system for maximum transmittance T_0, which is much less than the possible stopping frequency we get from a classical resonator. The bandwidth of REVI can be calculated as [35]

$$BW = \frac{\omega_{s2} - \omega_{s1}}{\sqrt{\omega_{s1}\,\omega_{s2}}} = \frac{f_{s2} - f_{s1}}{\sqrt{f_{s1}\,f_{s2}}} = 0.1767 \tag{36}$$

5.1. Experimental validation

A harmonic monochromatic sinusoidal base excitation of frequency range 20 Hz to 160 Hz is provided to the REVI through the dynamic shaker. The acceleration time histories and their corresponding frequency domain plots can be obtained using the procedure defined in subsection 4.1. The ratio of peak frequency amplitude of the bottom accelerometer to the top accelerometer ($\log_{10}(A_2/A_1)$), also known as transmittance, has been plotted in Figure 6 with blue circles. The transmittance calculated here is the ratio of acceleration in the u direction at nodes 2 and 1, which will be equal to velocity or displacement transmittance. Further, this experimental transmittance for the above frequency range is compared with the corresponding analytical displacement transmittance. From Figure 6, it is observed that the experimental transmittance values are successfully validated with the analytical transmittance of REVI, providing us essential confidence in our proposed methodology.

5.2. Parametric Study

The sensitivity of resonance and anti-resonance peaks in transmittance has been studied by varying the masses at nodes 2 and 3. The transmittance T_r has been plotted (Figure 7) for the following cases as

- The mass $m_2 = 0$ and mass $m_3 = 2^p\, m_r$, where p varies from -1 to 3 as shown in Figure 7 (a). It has been observed that resonance and anti-resonance occur at the same frequency. This frequency shifts to a lower frequency as the rigid mass m_3 increases. However, in this scenario, the width of the bandgap is too narrow.

- The mass $m_2 = 2^q\, m_r$ and mass $m_3 = m_r$, where q varies from 2 to 6 as shown in Figure 7 (b). It can be observed that by increasing mass at node 2, the resonating frequency of transmittance shifts to a lower frequency. However, the anti-resonance frequency does not change. So, it can be concluded that anti-resonance depends on the rigid mass of the REVI and not on the system's resting mass. The higher the mass ratio $\alpha = \frac{m_2}{m_3}$, the wider will be the band gap. However, the mid-frequency f_z depends on the rigid mass m_2.

- The mass $m_2 = 2^q\, m_r$ and mass $m_3 = 2^p\, m_r$, where where p varies from -2 to 2 and q varies from 2 to 6 as shown in Figure 7(c). Here, the mass ratio $\alpha = 2^4$ is constant. It can be seen that the resonance and anti-resonance both peaks shift towards a lower frequency range as the system's total mass increases. Similarly, it can be observed that the bandgap also gets wider for higher system mass.

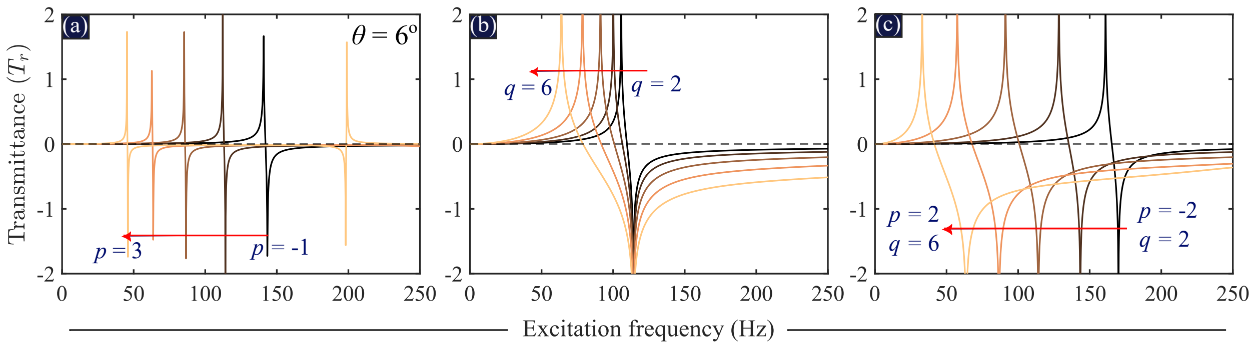

Figure 7: Variation of Transmittance (T_r) with the excitation frequency for different mass ratios. (a) The mass $m_2 = 0$ and mass $m_3 = 2^p\, m_r$, where p varies from -1 to 3, (b) The mass $m_2 = 2^q\, m_r$ and mass $m_3 = m_r$, where q varies from 2 to 6, (c) The mass $m_2 = 2^q\, m_r$ and mass $m_3 = 2^p\, m_r$, where where p varies from -2 to 2 and q varies from 2 to 6

5.2.1. Relative transmittance

Anti-resonance frequency is the critical parameter for designing the base isolator, as it determines the mid-frequency of the band gap. The following plots have been obtained Figure 8 by keeping the mass $m_3 = m_r$ constant and varying the mass $m_2 = 2^q$, where q increases from 0 to 2, for different transmittance, to obtain the rationale behind this anti-resonance phenomenon as follows.

- First of all the transmittance $T_r = \log_{10}(\frac{u_2}{u_1})$ has been plotted in Figure 8 (a). As discussed earlier, this demonstrates the constant f_z frequency with an increase in bandwidth as an increase in mass m_2.

- Further in Figure 8 (b), the transmittance of rigid mass m_3 in $T_{r1} = \log_{10}(\frac{u_3}{u_1})$ has been plotted. It can be noticed that the resonance frequencies are the same as that of

T_r, but the anti-resonance frequency is changed. The precise observation has noticed that all three cases' transmittance plots have one common point, which appears at the anti-resonance frequency f_z.

- The observation of common point motivated to obtain the transmittance of node 3 for node 2, to get the knowledge of the relative motion of masses m_3 and m_2. The Transmittance $T_{r2} = \log_{10}(\frac{u_3}{u_2})$ and Transmittance $T_{r3} = \log_{10}(\frac{v_3}{u_2})$ has been plotted in Figure 8 (c). In all three cases and both the transmittance T_{r2} and T_{r3}, the resonance frequency is the same as that of anti-resonance frequency f_z. So, it can be concluded that the anti-resonance of the system depends on the relative resonance of the base isolator concerning the load of the system resting on the isolator.

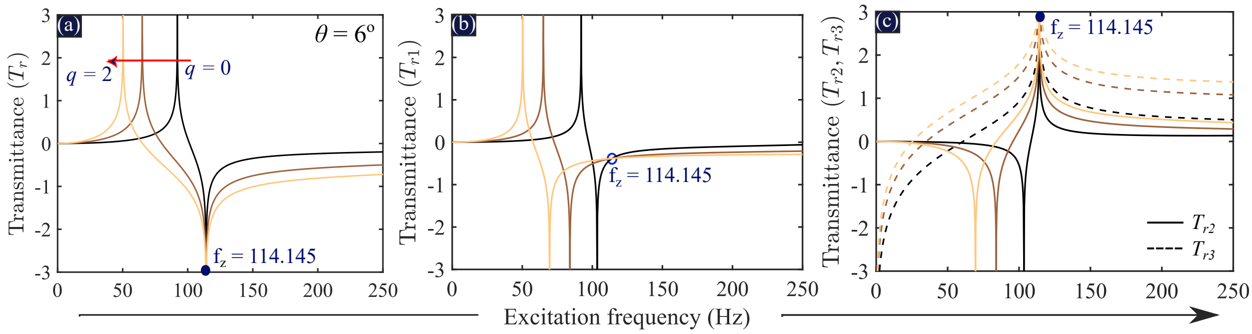

Figure 8: Variation of transmittance (T_r) and relative transmittance's (T_{r1}) and (T_{r2}) with the excitation frequency for different mass ratios. The mass $m_1 = 2^q\, m_a$ and mass $m_2 = m_r$, where q increases from 0 to 2 (a) Transmittance $T_r = \log_{10}(\frac{u_2}{u_1})$, (b) Transmittance $T_{r1} = \log_{10}(\frac{u_3}{u_1})$, (c) Transmittance $T_{r2} = \log_{10}(\frac{u_3}{u_2})$ and transmittance $T_{r3} = \log_{10}(\frac{v_3}{u_2})$. The resonance in relative transmittance results in antiresonance in transmittance (T_r).

5.2.2. Sensitivity to inclination angle

Further, a parametric study has been conducted showing the variation of transmittance as a function of excitation frequency for different values of inclination angle ($\theta = 20^o$, 30^o, 33.42^o, and 40^o) as illustrated in Figure 9 (a). Figure 9 (b) shows a contour plot about the negative transmittance profile (represented by negative values of transmittance plot in Figure 9 (a)) as a function of excitation frequency and inclination angle for enhanced comprehension of the bandgap and level of attenuation within the attenuation band. From Figure 9 (b), it can be observed that double anti-resonance peaks can be obtained in the attenuation band for inclination angles up to 33.41^o. The presence of two neighboring anti-resonances without an in-between resonance peak is noteworthy since this increases the bandwidth of the attenuation effect significantly [69]. For $\theta = 33.42^o$, the two attenuation peaks merge to form a single attenuation peak. Further, an increment of the angle creates the resonance cancellation phenomenon, completely vanishing the attenuation peaks and further reducing the band gap.

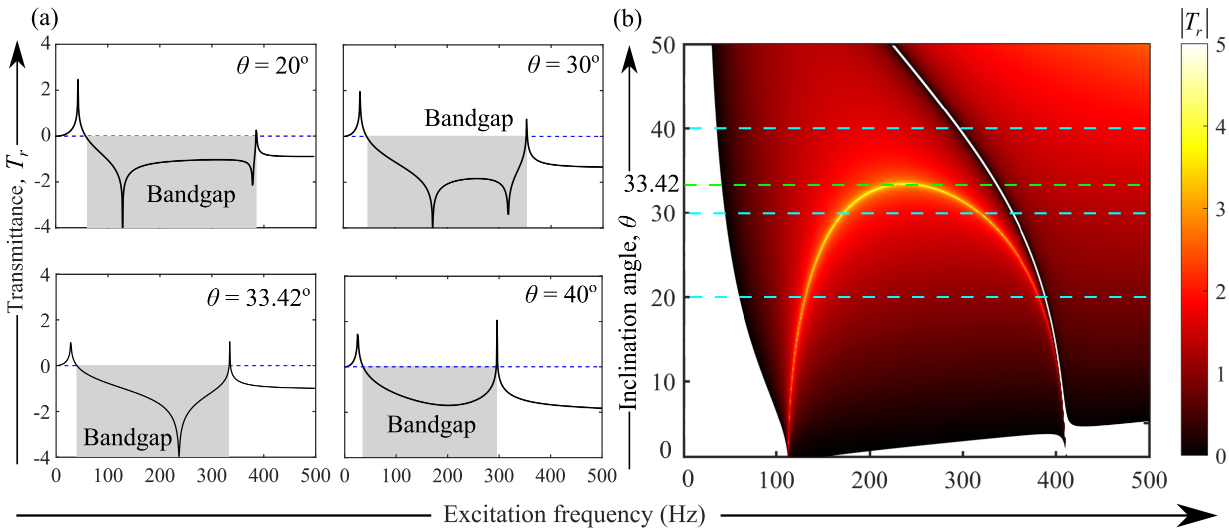

Figure 9: Effect of inclination angle on bandgap having node masses as 7.889x10^{-4} kg. (a) Transmittance plots for different values of inclination angle θ. (b) Attenuation profile (represented by negative values of transmittance plot) as a function of excitation frequency and inclination angle. In the attenuation band, double attenuation peaks can be obtained for inclination angles up to 33.41^o. For $\theta = 33.42^o$, the two attenuation peaks merge to form a single attenuation peak. Further, an increment of the angle creates the resonance cancellation phenomenon, completely vanishing the attenuation peaks and further reducing the band gap.

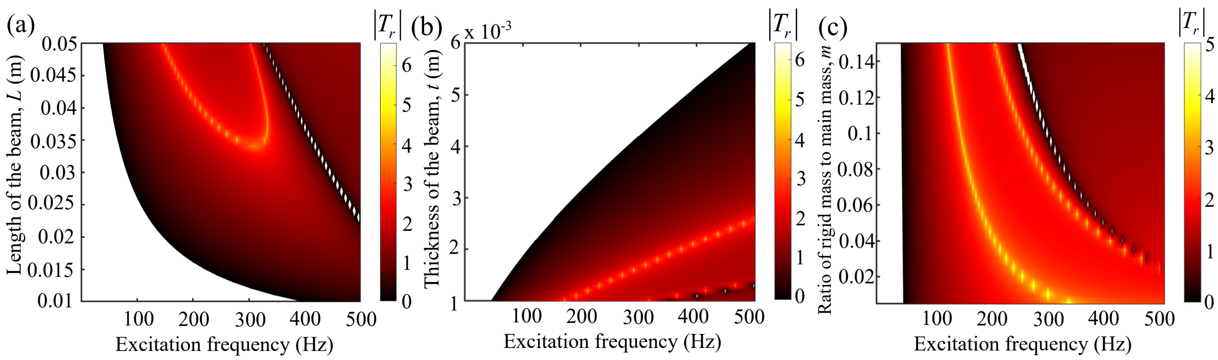

Figure 10: Attenuation profile (represented by negative values of transmittance plot) as a function of excitation frequency and several geometric parameters such as (a) Length of the beam. (b) The thickness of the beam. (c) The mass ratio (ratio of the rigid mass to the primary mass of the system).

5.2.3. Sensitivity of beam length, thickness, and nodal masses

The variation of the anti-resonance frequency of other geometric parameters of the REVI system has been observed using the contour plots shown in Figure 10. Figure 10 (a) to (c) shows the variation of negative transmittance profile (represented by negative values of transmittance) as a function of excitation frequency and three predominant geometric parameters such as length of the beams, the thickness of the beams and the nodal mass ratio. Figure 10 (a) depicts the emergence of double anti-resonance dips in the first band of REVI as we increase the length of the beam. Further, Figure 10 (b) showcases the linear change in the position of antiresonance dips as the change in beam thickness. Moreover, Figure 10 (c) demonstrates the double anti-resonance peaks in the first bandgap coming closer as the mass ratio increases. The main purpose of the contour plots is to decide the range of parameters that can be considered to achieve the desired anti-resonant frequencies.

5.2.4. Transmittance metrics and Relative bandgap

In continuation to subsubsection 5.2.3, to quantify the properties of the REVI band gap with double transmittance drops, three metrics are proposed as shown in Figure 11 (a) following [45]. The metric $\mu_{\min}$ denotes the minimum level of attenuation achieved within the double anti-resonance drops within the frequency range $\Omega_{\min}$ as illustrated in the figure. As for the metric $\Omega_{\max} = f_2 - f_1$, this represents the conventional band-gap width. In both frequency metrics, the bandwidth is normalized to its central frequency value, $\Omega_{\text{mid}} = \frac{f_1+f_2}{2}$. Upon normalization, $\Omega_{\min}$ and $\Omega_{\max}$ are denoted $\Omega^*_{\min}$ and $\Omega^*_{\max}$, respectively. The variation of metrics as a function of inclination angle is plotted in Figure 11 (b). The variation in transmittance level (blue curve) can be achieved for an inclination angle from 4 to 33.41 degrees. At 33.42 degrees, the double transmittance drops merge into a single drop, thus vanishing the transmittance level. Additionally, for an inclination angle less than 4 degrees, the range between the double peaks coincides with zero, thus again vanishing the transmittance level. Similarly, the red curve shows the maximum relative bandgap, which increases from 120 percent to 160 percent with an increase in inclination level. It is also observed that the minimum relative bandgap (black curve) decreases with the inclination angle, which shows a trade-off between different relative bandgaps.

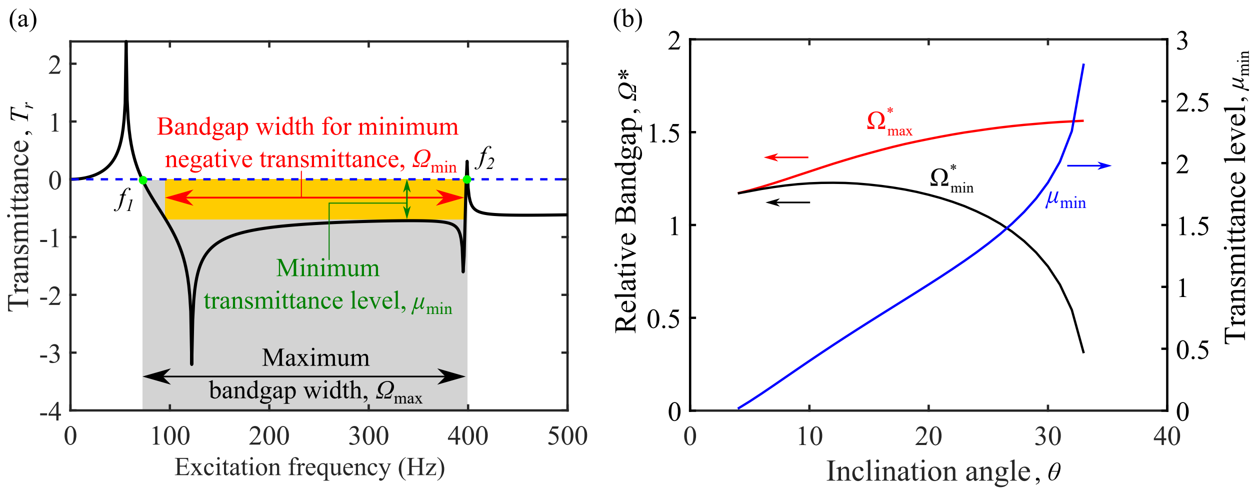

Figure 11: (a) Illustration of three metrics for the quantification of the relative bandgap size, minimum transmittance level, and relative band gap size corresponding to the minimum transmittance level; (b) Variation of the band-gap and transmittance metrics to inclination angle.

6. Conclusion

The dynamic response analysis of a base-excited novel monolithic rigid elastic vibration isolator (REVI) system has been conducted using analytical and experimental methods. The REVI model has been fabricated using a 3D printer. An analytical formulation of the proposed model is done by applying the spectral element method and rigid body dynamics concept. The displacement transmittance between the fixed and free end of the REVI has been validated experimentally, and a stop band of bandwidth of 0.1767 has been obtained for a maximum allowable transmittance of 0.25. The designed REVI gives a stop band in a frequency range lower than the equivalent classical spring mass resonator. The antiresonance phenomenon in REVI facilitates this occurrence of a lower-frequency stop band.

Moreover, parametric studies have been conducted by varying the masses to obtain the rationale behind the anti-resonance peak in transmittance. The higher the mass ratio α, widens the band gap, and the increase in the mass shifts the band towards the lower frequency range. The relative resonance of the rigid mass of REVI to the system's mass gives the antiresonance in the system transmittance. Additionally, an increment in the inclination angle θ enables us to obtain two neighboring anti-resonance peaks, significantly increasing the attenuation effect. The variation of θ also provides an insight into the bandwidth characteristics (horizontal and vertical) from which an optimum angle can be decided depending on the design requirement.

The primary novelty of the paper lies in fabricating a monolithic vibration isolator that uses the concept of rigid body dynamics and anti-resonance for broadband vibration isolation. The fabrication of the REVI is straightforward and without any manual connection. Therefore, this monolithic model has the benefits of repeatability and accuracy. Moreover, the analytical method is simple enough to apply in any modified version of the solved REVI system. Thus, the proposed REVI system can be a vibration isolator for the obtained stop band. In the future scope of this work, the proposed REVI type system can be applied in several real-life applications, such as automobiles and machine foundations where limited vibration transmittance is allowed.

7. Acknowledgements

The authors would like to acknowledge the research grant, namely:

- Core research grant, Science and Engineering Research Board, Department of Science and Technology (DST), Ministry of Science and Technology, Government of India, grant number CRG/2019/004696.
- Inspire faculty grant, Innovation in Science pursuit for Inspired Research, Department of Science and Technology (DST), Ministry of Science and Technology, Government of India, grant number DST/INSPIRE/04/2018/000052.

Additionally, the authors would like to acknowledge that a patent application related to the work described in this manuscript has been filed by the Indian Institute of Technology Delhi with the Indian Patent Office.

Appendix A. Reduced dynamic stiffness matrix ($\bar{\mathbf{K}}_{bc}$)

The global force-displacement relation derived can be written as per Eq. (28) as

$$\begin{bmatrix} F_{x1} \\ F_{y1} \\ M_1 \\ F_{x2} \\ F_{y2} \\ M_2 \\ F_{x3} \\ F_{y3} \\ M_3 \end{bmatrix} = \underbrace{\begin{bmatrix} \bar{K}_{11} & \bar{K}_{12} & & \cdots & \bar{K}_{19} \\ \bar{K}_{21} & \bar{K}_{22} & & & \\ & & & & \\ & & & & \\ \vdots & & & \ddots & \vdots \\ & & & & \\ & & & & \\ & & & & \\ \bar{K}_{91} & & \cdots & & \bar{K}_{99} \end{bmatrix}}_{\bar{\mathbf{K}}} \begin{bmatrix} u_1 \\ v_1 \\ \phi_1 \\ u_2 \\ v_2 \\ \phi_2 \\ u_3 \\ v_3 \\ \phi_3 \end{bmatrix} \tag{A.1}$$

Now, rearranging the global spectral element matrix ($\bar{\mathbf{K}}_{bc1}$) by separating known degrees of freedom (from boundary conditions given in Eq. (30)) as

$$\left[\begin{array}{c} F_{x1} \\ F_{x2} \\ M_2 \\ F_{x3} \\ F_{y3} \\ M_3 \\ \hline F_{y1} \\ M_1 \\ F_{y2} \end{array}\right] = \left[\begin{array}{c|c} \bar{\mathbf{K}}_{rr} & \bar{\mathbf{K}}_{rc} \\ \hline \bar{\mathbf{K}}_{cr} & \bar{\mathbf{K}}_{cc} \end{array}\right] \left[\begin{array}{c} u_1 \\ u_2 \\ \phi_2 \\ u_3 \\ v_3 \\ \phi_3 \\ \hline v_1 \\ \phi_1 \\ v_2 \end{array}\right] \tag{A.2}$$

Now, applying the static condensation to the Eq. (C.1), the condensed spectral element matrix ($\bar{\mathbf{K}}_{bc}$) can be obtained as

$$\bar{\mathbf{K}}_{bc} = \bar{\mathbf{K}}_{rr} \tag{A.3}$$

Appendix B. Reduced dynamic stiffness matrix ($\bar{\mathbf{K}}_{bc1}$)

Now, rearranging the global spectral element matrix $\bar{\mathbf{K}}$ by separating known degrees of freedom as per boundary conditions ($u_1 = v_1 = \phi_1 = v_2 = 0$)

$$\begin{bmatrix} F_{x2} \\ M_2 \\ F_{x3} \\ F_{y3} \\ M_3 \\ \hline F_{x1} \\ F_{y1} \\ M_1 \\ F_{y2} \end{bmatrix} = \left[\begin{array}{c|c} \bar{\mathbf{K}}_{rr} & \bar{\mathbf{K}}_{rc} \\ \hline \bar{\mathbf{K}}_{cr} & \bar{\mathbf{K}}_{cc} \end{array}\right] \begin{bmatrix} u_2 \\ \phi_2 \\ u_3 \\ v_3 \\ \phi_3 \\ \hline u_1 \\ v_1 \\ \phi_1 \\ v_2 \end{bmatrix} \tag{B.1}$$

Now, applying the static condensation to the Eq. (B.1), the condensed spectral element matrix ($\bar{\mathbf{K}}_{bc1}$) can be obtained as

$$\bar{\mathbf{K}}_{bc1} = \bar{\mathbf{K}}_{rr} \tag{B.2}$$

Appendix C. Reduced force displacement equation for transmittance study

Applying the boundary conditions of zero displacements, the dynamic force-displacement equation can be written as per Eq. (31). Further, the obtained dynamic stiffness matrix Eq. (A.3) has been divided into four parts as per known and unknown degrees of freedom as follows

$$\begin{bmatrix} F_{x1} \\ \hline F_{x2} \\ M_2 \\ F_{x3} \\ F_{y3} \\ M_3 \end{bmatrix} = \left[\begin{array}{c|c} \bar{K}_{11} & \bar{\mathbf{K}}_{1r} \\ \hline \bar{\mathbf{K}}_{r1} & \bar{\mathbf{K}}_{rr} \end{array}\right] \begin{bmatrix} u_1 = 1 \\ \hline u_2 \\ \phi_2 \\ u_3 \\ v_3 \\ \phi_3 \end{bmatrix} \tag{C.1}$$

$$\longrightarrow \begin{bmatrix} F_{x1} \\ \mathbf{F}_r \end{bmatrix} = \begin{bmatrix} \bar{K}_{11} & \bar{\mathbf{K}}_{1r} \\ \bar{\mathbf{K}}_{r1} & \bar{\mathbf{K}}_{rr} \end{bmatrix} \begin{bmatrix} 1 \\ \mathbf{u}_r \end{bmatrix}$$

Finally, the reduced force-displacement equation can be written as

$$\mathbf{F}_r = \bar{\mathbf{K}}_{r1} + \bar{\mathbf{K}}_{rr}\,\mathbf{u}_r \tag{C.2}$$

References

[1] A. P. Meran, Numerical analysis of elastomer buffer embedded in the suspension of automobile for vibration damping improvement, International Journal of Automotive Engineering and Technologies 7 (1) (2018) 65–75.

[2] K. V. S. Prasad, V. Nagasai, J. S. S. Laxman, K. A. Kumar, P. R. Sreekanth, Stainless steel wave spring as vibration absorber for motorcycle: Design simulation and analysis, Materials Today: Proceedings 56 (2022) 1056–1062.

[3] A. Rita, J. McGarvey, R. Jones, Helicopter rotor isolation evaluation utilizing the dynamic antiresonant vibration isolator, Journal of the American Helicopter Society 23 (1) (1978) 22–29.

[4] D. Braun, Development of antiresonance force isolators for helicopter vibration reduction, Journal of the American Helicopter Society 27 (4) (1982) 37–44.

[5] A. Tamer, V. Muscarello, P. Masarati, G. Quaranta, Evaluation of vibration reduction devices for helicopter ride quality improvement, Aerospace Science and Technology 95 (2019) 105456.

[6] M. A. Hawwa, Vibration isolation of machine foundations by periodic trenches, Journal of engineering mechanics 124 (4) (1998) 422–427.

[7] V. Ivovich, M. Savovich, Isolation of floor machines by lever-type inertial vibration corrector, Proceedings of the Institution of Civil Engineers-Structures and Buildings 146 (4) (2001) 391–402.

[8] A. Kampitsis, K. Kapasakalis, L. Via-Estrem, An integrated fea-cfd simulation of offshore wind turbines with vibration control systems, Engineering Structures 254 (2022) 113859.

[9] R. Kandasamy, F. Cui, N. Townsend, C. C. Foo, J. Guo, A. Shenoi, Y. Xiong, A review of vibration control methods for marine offshore structures, Ocean Engineering 127 (2016) 279–297.

[10] D. Newland, H. Hunt, Isolation of buildings from ground vibration: a review of recent progress, Proceedings of the Institution of Mechanical Engineers, Part C: Mechanical Engineering Science 205 (1) (1991) 39–52.

[11] A. Saha, S. K. Mishra, Adaptive negative stiffness device based nonconventional tuned mass damper for seismic vibration control of tall buildings, Soil Dynamics and Earthquake Engineering 126 (2019) 105767.

[12] G. Bhansali, G. Singh, et al., Novel viscoelastic vibration isolating methods in space technology: A review, Materials Today: Proceedings (2022).

[13] M. Oddiraju, A. Behjat, M. Nouh, S. Chowdhury, Inverse design framework with invertible neural networks for passive vibration suppression in phononic structures, Journal of Mechanical Design 144 (2) (2022).

[14] S. Chowdhury, A. Banerjee, S. Adhikari, Enhanced seismic base isolation using inertial amplifiers, in: Structures, Vol. 33, Elsevier, 2021, pp. 1340–1353.

[15] S. Chowdhury, A. Banerjee, S. Adhikari, Optimal negative stiffness inertial-amplifier-base-isolators: Exact closed-form expressions, International Journal of Mechanical Sciences 218 (2022) 107044.

[16] S. Chowdhury, A. Banerjee, The exact closed-form expressions for optimal design parameters of resonating base isolators, International Journal of Mechanical Sciences 224 (2022) 107284.

[17] S. Chowdhury, A. Banerjee, S. Adhikari, Optimal design of inertial amplifier base isolators for dynamic response control of multi-storey buildings, International Journal of Structural Stability and Dynamics (2022) 2350047.

[18] L. Arany, S. Bhattacharya, J. Macdonald, S. J. Hogan, Simplified critical mudline bending moment spectra of offshore wind turbine support structures, Wind Energy 18 (12) (2015) 2171–2197.

[19] X. Han, W. Qiao, B. Zhou, Frequency domain response of jacket platforms under random wave loads, Journal of Marine Science and Engineering 7 (10) (2019) 328.

[20] A. Banerjee, T. Chakraborty, V. Matsagar, M. Achmus, Dynamic analysis of an offshore wind turbine under random wind and wave excitation with soil-structure interaction and blade tower coupling, Soil Dynamics and Earthquake Engineering 125 (2019) 105699.

[21] J. Liu, L. Ju, D. G. Blair, Vibration isolation performance of an ultra-low frequency folded pendulum resonator, Physics Letters A 228 (4-5) (1997) 243–249.

[22] Z. Cheng, Z. Shi, Vibration attenuation properties of periodic rubber concrete panels, Construction and Building Materials 50 (2014) 257–265.

[23] S. J. Mitchell, A. Pandolfi, M. Ortiz, Metaconcrete: designed aggregates to enhance dynamic performance, Journal of the Mechanics and Physics of Solids 65 (2014) 69–81.

[24] S. Kim, Y.-H. Kim, J.-H. Jang, A theoretical model to predict the low-frequency sound absorption of a helmholtz resonator array, The Journal of the Acoustical Society of America 119 (4) (2006) 1933–1936.

[25] F. Simon, Long elastic open neck acoustic resonator for low frequency absorption, Journal of Sound and Vibration 421 (2018) 1–16.

[26] A. Banerjee, Influence of the torsional vibration of the periodically attached perpendicular beam resonator on the flexural band of a euler-bernoulli beam, Physics Letters A 384 (29) (2020) 126757.

[27] Z. Zhao, Q. Chen, R. Zhang, C. Pan, Y. Jiang, Energy dissipation mechanism of inerter systems, International Journal of Mechanical Sciences 184 (2020) 105845.

[28] J. Zhou, L. Dou, K. Wang, D. Xu, H. Ouyang, A nonlinear resonator with inertial amplification for very low-frequency flexural wave attenuations in beams, Nonlinear Dynamics 96 (1) (2019) 647–665.

[29] G. Yan, J.-J. Lu, W.-H. Qi, T.-Y. Zhao, H. Yan, L.-C. Zhao, Z.-Y. Wu, W.-M. Zhang, Tetrahedron structure with nonlinear stiffness and inertia modulation for enhanced low frequency vibration isolation, Journal of Sound and Vibration (2023) 117897doi:https://doi.org/10.1016/j.jsv.2023.117897. URL https://www.sciencedirect.com/science/article/pii/S0022460X23003462

[30] Y. Liu, D. Chronopoulos, J. Yang, Vibration power flow and wave transmittance analysis of inerter-based dual-resonator acoustic metamaterial, in: International Conference on Wave Mechanics and Vibrations, Springer, 2023, pp. 966–975.

[31] J. S. Jensen, Phononic band gaps and vibrations in one-and two-dimensional mass–spring structures, Journal of sound and Vibration 266 (5) (2003) 1053–1078.

[32] R. Belotti, D. Richiedei, I. Tamellin, Antiresonance assignment in point and cross receptances for undamped vibrating systems, Journal of Mechanical Design 142 (2) (2020).

[33] N. Liu, Z. Jin, H. Hua, A new model of a hydraulic leveraged dynamic anti-resonance vibration isolator under base excitation: A theoretical and experimental study, Journal of Vibration and Control 25 (16) (2019) 2282–2292.

[34] N. Duan, H. Yu, X. Ma, Z. Zhang, H. Hua, Experimental investigations on the hydraulic leveraged dynamic anti-resonance vibration isolator under base excitation, in: INTER-NOISE and NOISE-CON Congress and Conference Proceedings, Vol. 261, Institute of Noise Control Engineering, 2020, pp. 4311–4319.

[35] C. Yilmaz, N. Kikuchi, Analysis and design of passive band-stop filter-type vibration isolators for low-frequency applications, Journal of Sound and Vibration 291 (3-5) (2006) 1004–1028.

[36] H.-P. Lin, D. Yang, Dynamic responses of two beams connected by a spring-mass device, Journal of Mechanics 29 (1) (2013) 143–155.

[37] Y. Zhang, X. Fan, J. Li, F. Li, G. Yu, R. Zhang, K. Yuan, Low-frequency vibration insulation performance of the pyramidal lattice sandwich metamaterial beam, Composite Structures 278 (2021) 114719.

[38] H. Bao, C. Wu, K. Wang, B. Yan, An enhanced dual-resonator metamaterial beam for low-frequency vibration suppression, Journal of Applied Physics 129 (9) (2021) 095106.

[39] C. Yilmaz, G. M. Hulbert, N. Kikuchi, Phononic band gaps induced by inertial amplification in periodic media, Physical Review B 76 (5) (2007) 054309.

[40] C. Yilmaz, G. Hulbert, Theory of phononic gaps induced by inertial amplification in finite structures, Physics Letters A 374 (34) (2010) 3576–3584.

[41] Z. Dong, P. Sheng, Inertial-amplified mechanical resonators for the mitigation of ultralow-frequency vibrations, Physical Review Applied 18 (1) (2022) 014027.

[42] J. Wu, L. Zeng, B. Han, Y. Zhou, X. Luo, X. Li, X. Chen, W. Jiang, Analysis and design of a novel arrayed magnetic spring with high negative stiffness for low-frequency vibration isolation, International Journal of Mechanical Sciences 216 (2022) 106980.

[43] G. Hu, L. Tang, J. Xu, C. Lan, R. Das, Metamaterial with local resonators coupled by negative stiffness springs for enhanced vibration suppression, Journal of Applied Mechanics 86 (8) (2019) 081009.

[44] Y. Liu, X. Su, C. Sun, Broadband elastic metamaterial with single negativity by mimicking lattice systems, Journal of the Mechanics and Physics of Solids 74 (2015) 158–174.

[45] A. Banerjee, S. Adhikari, M. I. Hussein, Inertial amplification band-gap generation by coupling a levered mass with a locally resonant mass, International Journal of Mechanical Sciences 207 (2021) 106630.

[46] A. Bhatt, A. Banerjee, Double attenuation peaks in metamaterial with simultaneous negative mass and stiffness, Physics Letters A (2022) 128201.

[47] Y. Liu, J. Yang, X. Yi, D. Chronopoulos, Enhanced suppression of low-frequency vibration transmission in metamaterials with linear and nonlinear inerters, Journal of Applied Physics 131 (10) (2022) 105103.

[48] G. Huang, C. Sun, Band gaps in a multiresonator acoustic metamaterial, Journal of Vibration and Acoustics 132 (3) (2010).

[49] D. Kamesh, R. Pandiyan, A. Ghosal, Passive vibration isolation of reaction wheel disturbances using a low frequency flexible space platform, Journal of sound and vibration 331 (6) (2012) 1310–1330.

[50] J. Li, S. Cao, J. Zheng, On the characteristic of a small-scale isolation mechanism with three-dimensional quasi-zero stiffness, Journal of Mechanical Design 142 (9) (2020) 095001.

[51] M. M. Khan, D. C. Lagoudas, J. J. Mayes, B. K. Henderson, Pseudoelastic sma spring elements for passive vibration isolation: Part i–modeling, Journal of Intelligent Material Systems and Structures 15 (6) (2004) 415–441.

[52] H. Li, Y. Li, J. Li, Negative stiffness devices for vibration isolation applications: a review, Advances in Structural Engineering 23 (8) (2020) 1739–1755.

[53] S. Zuo, D. Wang, Y. Zhang, Q. Luo, Design and testing of a parabolic cam-roller quasi-zero-stiffness vibration isolator, International Journal of Mechanical Sciences 220 (2022) 107146.

[54] K. Kocak, C. Yilmaz, Design of a compliant lever-type passive vibration isolator with quasi-zero-stiffness mechanism, Journal of Sound and Vibration 558 (2023) 117758. `doi:https://doi.org/10.1016/j.jsv.2023.117758`.
URL `https://www.sciencedirect.com/science/article/pii/S0022460X23002079`

[55] K. Mizukami, K. Funaba, K. Ogi, Design and three-dimensional printing of carbon-fiber-composite elastic metamaterials with inertial amplification mechanisms, Journal of Sound and Vibration 513 (2021) 116412.

[56] M. Sun, G. Song, Y. Li, Z. Huang, Effect of negative stiffness mechanism in a vibration isolator with asymmetric and high-static-low-dynamic stiffness, Mechanical Systems and Signal Processing 124 (2019) 388–407.

[57] G. Acar, C. Yilmaz, Experimental and numerical evidence for the existence of wide and deep phononic gaps induced by inertial amplification in two-dimensional solid structures, Journal of Sound and Vibration 332 (24) (2013) 6389–6404.

[58] S. Taniker, C. Yilmaz, Generating ultra wide vibration stop bands by a novel inertial amplification mechanism topology with flexure hinges, International Journal of Solids and Structures 106 (2017) 129–138.

[59] M.-Q. Niu, L.-Q. Chen, Analysis of a bio-inspired vibration isolator with a compliant limb-like structure, Mechanical Systems and Signal Processing 179 (2022) 109348.

[60] K. H. Matlack, A. Bauhofer, S. Krödel, A. Palermo, C. Daraio, Composite 3d-printed metastructures for low-frequency and broadband vibration absorption, Proceedings of the National Academy of Sciences 113 (30) (2016) 8386–8390.

[61] W. Elmadih, D. Chronopoulos, W. Syam, I. Maskery, H. Meng, R. Leach, Three-dimensional resonating metamaterials for low-frequency vibration attenuation, Scientific reports 9 (1) (2019) 1–8.

[62] T. Ampatzidis, R. K. Leach, C. Tuck, D. Chronopoulos, Band gap behaviour of optimal one-dimensional composite structures with an additive manufactured stiffener, Composites Part B: Engineering 153 (2018) 26–35.

[63] L. D'Alessandro, R. Ardito, F. Braghin, A. Corigliano, Low frequency 3d ultra-wide vibration attenuation via elastic metamaterial, Scientific reports 9 (1) (2019) 1–8.

[64] S. K. Arul Prakash, T. Mahan, G. Williams, C. McComb, J. Menold, C. S. Tucker, Detection of system compromise in additive manufacturing using video motion magnification, Journal of Mechanical Design

142 (3) (2020).
[65] A. Banerjee, R. Das, E. P. Calius, Waves in structured mediums or metamaterials: a review, Archives of Computational Methods in Engineering 26 (4) (2019) 1029–1058.
[66] Vedant, J. T. Allison, Pseudo-rigid-body dynamic models for design of compliant members, Journal of Mechanical Design 142 (3) (2020) 031116.
[67] X. Liu, C. Sun, J. R. Banerjee, H.-C. Dan, L. Chang, An exact dynamic stiffness method for multibody systems consisting of beams and rigid-bodies, Mechanical Systems and Signal Processing 150 (2021) 107264.
[68] A. Bhatt, A. Banerjee, Flexural wave propagation in rigid elastic combined metabeam, Journal of Vibration and Acoustics (2022) 1–31.
[69] M. I. Hussein, I. Patrick, A. Banerjee, S. Adhikari, Metadamping in inertially amplified metamaterials: Trade-off between spatial attenuation and temporal attenuation, Journal of Sound and Vibration 531 (2022) 116977.